

# Weak lensing scattering transform: dark energy and neutrino mass sensitivity

Sihao Cheng (程思浩)<sup>1\*</sup> & Brice Ménard<sup>1</sup>

<sup>1</sup>*Department of Physics and Astronomy, The Johns Hopkins University, 3400 N Charles Street, Baltimore, MD 21218, USA*

1 March 2025

## ABSTRACT

As weak lensing surveys become deeper, they reveal more non-Gaussian aspects of the convergence field which require statistics beyond the power spectrum to extract. In Cheng et al. (2020), we showed that the scattering transform, a novel statistic borrowing concepts from convolutional neural networks, is a powerful tool to perform cosmological parameter estimation. Here, we extend this analysis to explore its sensitivity to dark energy and neutrino mass parameters with weak lensing surveys. We first use image synthesis to show visually that the scattering transform provides a better statistical vocabulary to characterize lensing mass maps compared to the power spectrum and bispectrum. We then show that it outperforms those two estimators in the low-noise regime. When the noise level increases and non-Gaussianity is diluted, though the constraint is not significantly tighter than that of the bispectrum, the scattering coefficients have much more Gaussian likelihood, which is essential for accurate cosmological inference. We argue that the scattering coefficients are preferred statistics considering both constraining power and likelihood properties.

**Key words:** methods: statistical – gravitational lensing: weak – cosmological parameters – large-scale structure of Universe

## 1 INTRODUCTION

Statistical properties of matter density distribution in our Universe carry information about its components and evolutionary history. In the late-time universe probed by weak gravitational lensing distortion, or cosmic shear (see Bartelmann & Schneider 2001; Kilbinger 2015, for reviews), the non-linear growth of structure imprints non-Gaussianity at small scales. As a result, cosmological information starts to elude Gaussian statistics such as the power spectrum and correlation function (Rimes & Hamilton 2005, 2006; Neyrinck et al. 2006; Neyrinck & Szapudi 2007). To extract more information, some non-Gaussian statistics, such as the bispectrum (Fu et al. 2014), peak counts (Liu et al. 2015a,b; Kacprzak et al. 2016; Martinet et al. 2018; Shan et al. 2018), and Minkowski functionals (Petri et al. 2015), have been applied to existing weak lensing data. Deeper ongoing and future surveys like the Hyper Suprime-Cam survey (HSC, Aihara et al. 2018a,b), Rubin Observatory survey (formerly LSST, LSST Science Collaboration et al. 2009), *Euclid* (Laureijs et al. 2011), and Roman space telescope survey (formerly WFIRST, Spergel et al. 2015) have access to even smaller scales, making it increasingly important to employ proper statistics that can capture the non-Gaussian information in lensing maps (see, e.g., Martinet et al. 2021, and reference therein).

In Cheng et al. (2020), we proposed to use a non-Gaussian statistical tool that is novel to cosmology: the scattering transform<sup>1</sup>. We demonstrated its power by applying it to simulated weak lens-

ing maps to constrain the  $\Omega_m$  and  $\sigma_8$  cosmological parameters. In this companion paper, we extend our analysis to other cosmological dependencies: the dark energy equation of state  $w_0$ ,  $w_a$  and the neutrino mass sum  $M_\nu$ . Constraining these parameters is one of the key goals of upcoming weak lensing surveys and they are often used in the figure of merits to compare different survey strategies.

The scattering transform, introduced by (Mallat 2012) in the signal processing literature, uses concepts found in convolutional neural networks, but it needs no training: similar to traditional statistical estimators, it generates a set of summary statistics, which efficiently characterize complex non-Gaussianity at various scales. To visualize the power of scattering coefficients, we will first show that one can use them to generate random images with textures very similar to real lensing maps, to a level not achievable by traditional moment-based statistics such as the power spectrum and bispectrum. Then, we will present the constraining power of scattering coefficients for dark energy parameters and neutrino mass.

## 2 SCATTERING TRANSFORM

The scattering transform (Mallat 2012; Bruna & Mallat 2013) was originally developed in the context of signal processing in computer vision (see, e.g., Sifre & Mallat 2013; Andén & Mallat 2014; Bruna et al. 2015). In astrophysics, it has been used for parameter inference in cosmology (Cheng et al. 2020) and analysis of interstellar medium (Allys et al. 2019; Saydjari et al. 2020).

The scattering transform shares some properties with both convolutional neural networks (CNNs) and  $N$ -point correlation functions in desirable ways: it is powerful at extracting information from com-

\* E-mail: s.cheng@jhu.edu

<sup>1</sup> To our best knowledge, the scattering transform has nothing to do with the scattering process in particle physics.

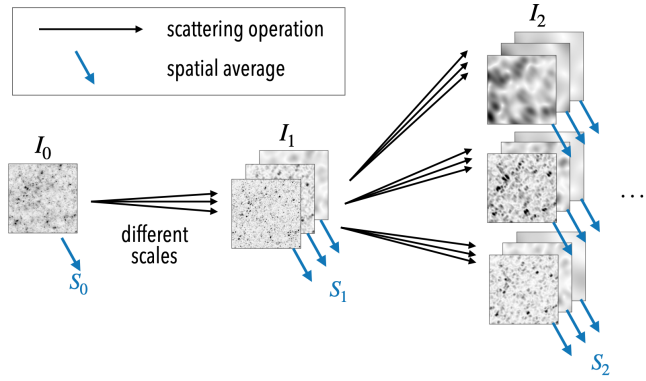


**Figure 1.** Structure of the scattering transform. From the input signal, a tree of intermediate signals are generated by iterating the scattering operation, then the spatial averages of these images, are taken as the translational invariant scattering coefficients. The scattering operation is composed of a wavelet convolution and a pixelwise modulus.

plex non-Gaussian fields, but it is deterministic, interpretable, and does not require any training. It compresses information into a relatively small set of coefficients due to its relation to wavelets, and it is a ‘first-order’ statistic, i.e. it never amplifies the fluctuations present in the input.

On the one hand, the scattering transform can be understood as a CNN with pre-determined, non-trainable kernels. It inherits CNN’s way to extract spatial patterns, including local convolutions, a non-amplifying nonlinear operation, and iterations, but it abandons the learning ability which makes CNNs less controllable or interpretable.

On the other hand, the scattering transform is also similar to  $N$ -point functions averaged within wide, logarithmically-spaced bins (Cheng et al. 2020). But, instead of using the multiplication of  $N$  field intensities, the scattering transform uses a non-amplifying nonlinear operation to convert field fluctuations into their strengths. Therefore, the scattering transform does not amplify the tail of the underlying distribution function and thus alleviates the corresponding information loss problem described by Carron (2011, 2012); Carron & Neyrinck (2012).

## 2.1 Formulation

The mathematics of scattering transform was introduced in Mallat (2012); Bruna & Mallat (2013). Here, we present a succinct introduction, following the notation in our first paper (Cheng et al. 2020). In brief, the scattering transform extracts information from a field by applying the following operations:

- wavelet convolution + modulus
- iteration
- spatial average

It can be formalized in a recursive way, as illustrated in Figure 1:

$$I_0 \equiv \text{input field} \quad (1)$$

$$I_n^{j,l} \equiv \left| I_{n-1} \star \psi^{j,l} \right| \quad (\text{the scattering operation}) \quad (2)$$

$$S_n \equiv \langle I_n \rangle, \quad (3)$$

where  $\psi^{j,l}$  stands for a wavelet indexed by its scale  $j$  and orientation  $l$ .

The scattering operation is composed of a wavelet convolution followed by a pixelwise modulus. The function of convolution  $\star \psi^{j,l}$  is

to separate fluctuations into different scales; the function of modulus  $|\cdot|$  is to convert the selected fluctuations into their local strengths. Iterations of the scattering operation then form a tree structure, i.e. a planar network, with various scattering fields  $I_n$  at its nodes. Each  $I_n$  is the intensity map of fluctuations of a particular scale in the previous-order field  $I_{n-1}$ . It can also be understood as a non-linear intensity map of a certain pattern in the input image  $I_0$ .

Finally, the translation-invariant scattering coefficients  $S$  are defined as the spatial average of every scattering image, which resembles the pooling operation in convolutional neural networks. In this way, the 0th-, 1st-, and 2nd-order scattering coefficients can be written explicitly as:

$$S_0 \equiv \langle I_0 \rangle \quad (4)$$

$$S_1^{j_1, l_1} \equiv \langle I_1^{j_1, l_1} \rangle = \langle |I_0 \star \psi^{j_1, l_1}| \rangle \quad (5)$$

$$S_2^{j_1, l_1, j_2, l_2} \equiv \langle I_2^{j_1, l_1, j_2, l_2} \rangle = \langle |I_0 \star \psi^{j_1, l_1} \star \psi^{j_2, l_2}| \rangle. \quad (6)$$

The scattering operation which separates scales and measures fluctuation strength is qualitatively similar to the power spectrum analysis. Indeed, if we replace the modulus in Equation 2 by modulus squared, the scattering coefficients  $S_n$  will exactly become averaged  $2^n$ -point functions weighted by a sequence of wavelets. However, the modulus instead of modulus squared makes it much more efficient in extracting information from the tail of the field probability distribution function (PDF). A more in-depth discussion will be presented in Cheng et al. (in preparation).

The number of scattering coefficients  $S_n$  is determined by the number of distinct wavelets used. Using  $J$  scales and  $L$  orientations, the total number of coefficients up to the 2nd order is  $1 + JL + J(J-1)L^2/2$ . If orientation does not provide much relevant information, one may average over the directional indices:

$$s_n \equiv \langle S_n \rangle_{l_1, \dots, l_n}, \quad (7)$$

which reduces the number of coefficients to  $1 + J + J(J-1)/2$ , up to the 2nd order. For example, when using dyadic wavelets, a  $512 \times 512$  pixel image has 8 wavelet scales ( $J = 8$ ), corresponding to only 37 reduced scattering coefficients.

For more intuitive understanding of the scattering transform and coefficients, we refer the readers to Cheng et al. (2020) and Cheng et al. (in prep.); For more mathematical properties, we refer the readers to Mallat (2012) and Bruna et al. (2015).

## 2.2 Image generation based on scattering coefficients

To compare the performance of different statistics in characterizing a random field, it is informative to compare them through their image synthesis capabilities. Here we will focus on three statistics: the power spectrum, the bispectrum and the scattering coefficients in the context of weak lensing convergence maps. The idea of synthesis is to randomly generate new images (or, in other words, to sample from the ensemble of images) that have the same summary statistics as the target one, and then visually check the *texture* of the generated images (see, e.g., Bruna & Mallat 2019; Allys et al. 2020).

To implement it, we start from a random image and modify it in order to minimize the difference of the summary statistics between the generated and the target images. Technically, we start from a Gaussian random field that has the same power spectrum as the target image, and then use the ‘adam’ optimizer in the python package `torch.optim` to minimize a loss function defined from the difference of summary statistics between the generated and target image. In the scattering coefficient and bispectrum cases, we also minimize

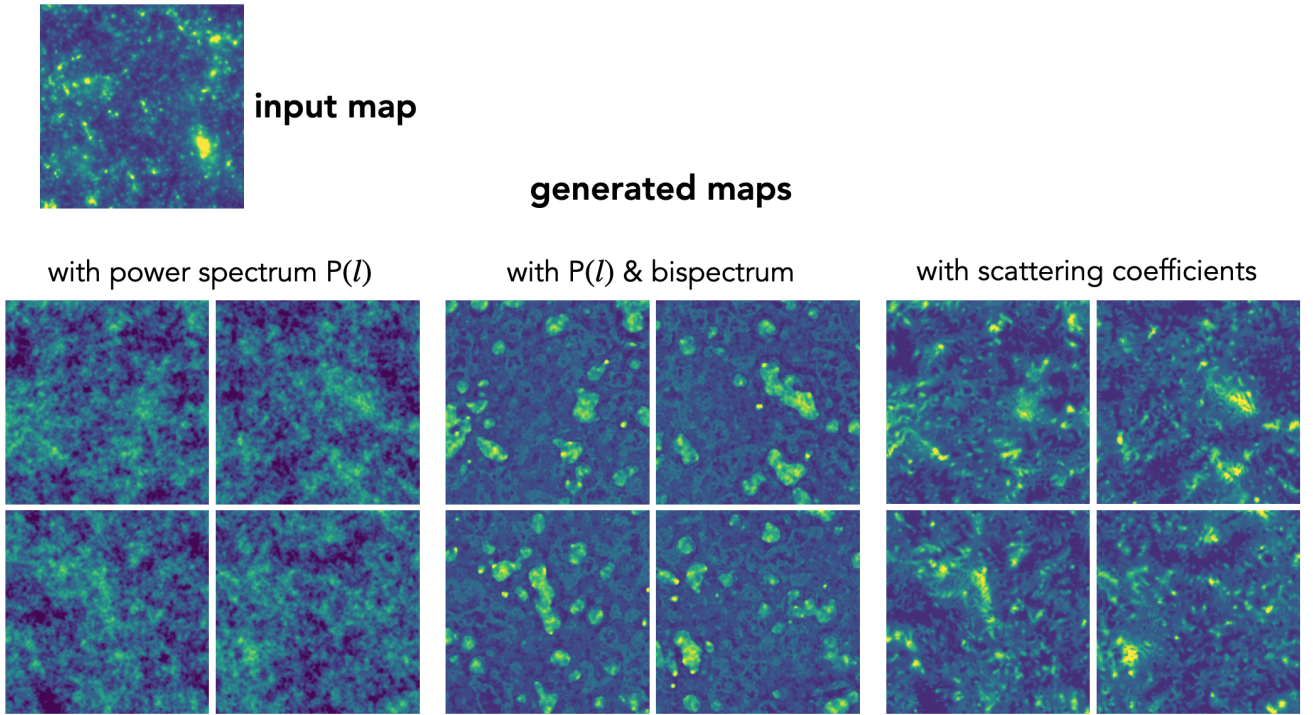


**Figure 2.** Images generated with selected sets of summary statistics, including the power spectrum, bispectrum, and scattering coefficients ( $S_1$ ,  $S_2$ ), showing that the scattering coefficients characterize the field better. As the image generation is random, one should compare textures, instead of the exact positions of features, between the input and generated maps.

the difference of their  $L_1$  norms and set a lower bound for all pixels. Our code for image generation is available online<sup>2</sup>.

In Figure 2, we show the generated images using power spectrum  $P$ , bispectrum  $B$ , and the scattering coefficients  $S$ . For each set of statistics, four realizations are shown to illustrate the sampling variance. Compared to the power spectrum and bispectrum, the results from scattering coefficients look much more similar to a real lensing convergence map (target image), especially in the textures created by halos on all scales.

There are several caveats about image synthesis to keep in mind. For example, the image quality somewhat depends on the initial condition and the choice of loss function. More importantly, the concept of information must always be related to a particular task. In the image synthesis case, this task is ‘to distinguish fields under the metric of human eyes and brains’, which can be different from the Fisher information in the cosmological parameter inference task. Nevertheless, the striking visual similarity between the target and generated images using scattering coefficients is evidence of their power to characterize lensing map textures.

### 3 COSMOLOGICAL FORECAST

To explore the constraining power of the scattering coefficients on cosmological parameters, we calculate the Fisher forecast (Fisher 1935; Vogeley & Szalay 1996; Tegmark et al. 1997) and Bayesian posterior of the cosmological parameters, after building a likelihood emulator for the scattering coefficients using simulated lensing convergence maps.

### 3.1 Simulated lensing maps

To explore the effects of dark energy and neutrino mass on lensing scattering coefficients, we use two sets of simulated convergence maps, which were generously made available by the Columbia lensing team<sup>3</sup>. Both datasets were designed for probing the non-Gaussian information in weak lensing cosmology. The convergence maps were produced through ray-tracing  $N$ -body simulations to certain source redshifts without the Born approximation, using the `Lenstools` python package (Petri 2016). All the cosmologies are spatially flat. The first dataset, described in Petri (2016); Zorrilla Matilla et al. (2016); Liu et al. (2016), varies dark energy properties and matter density ( $w_0$ ,  $w_a$ , and  $\Omega_m$ ). The convergence is traced to one source redshift ( $z = 2$ ). The second dataset, MassiveNuS (Liu et al. 2018), varies neutrino mass, matter density, and primordial fluctuation amplitude ( $M_\nu$ ,  $\Omega_m$ , and  $A_s$ , equivalent to  $M_\nu$ ,  $\Omega_m$ , and  $\sigma_8$ ), and the convergence is traced to five source redshifts ( $z = 0.5, 1, 1.5, 2, 2.5$ ). Both datasets contain multiple realizations of convergence maps in multiple cosmologies, with  $3.5 \times 3.5 \text{ deg}^2$  field of view (where non-linear gravitational evolution becomes important) and  $512 \times 512$  pixel resolution. Thus these maps cover multipole moments  $l$  from 100 to roughly 30,000. Below we describe these datasets in more detail.

**Dark Energy simulations:** This dataset contains simulations of 7  $w_0 w_a$  CDM cosmologies with different dark energy properties, including the present dark energy density  $\Omega_\Lambda$  and the dark energy equation of state index  $w(a)$ , parametrized by  $w_0$  and  $w_a$  through  $w(a) = w_0 + (1 - a)w_a$  (Chevallier & Polarski 2001). Each simulation was run in a  $240 \text{ Mpc}/h$  box with  $512^3$  particles and used to generate 1,024 mock convergence maps with  $3.5 \times 3.5 \text{ deg}^2$  field of view. The

<sup>2</sup> [https://github.com/SihaoCheng/scattering\\_transform](https://github.com/SihaoCheng/scattering_transform)

<sup>3</sup> <http://columbialensing.org>

lensing sources were set at redshift  $z = 2$ . We down-sampled the original  $2048^2$  pixel maps to a  $512^2$  resolution with 0.41 arcmin per pixel, by averaging adjacent pixels. Besides the dark energy properties, other cosmological parameters are fixed: baryon density  $\Omega_b = 0.046$ , Hubble constant  $h = 0.72$ , scalar spectral index  $n_s = 0.96$ , normalization of fluctuation amplitude  $\sigma_8 = 0.8$ , effective number of relativistic degrees of freedom  $n_{\text{eff}} = 3.04$ , total neutrino masses  $M_\nu = 0.0$ , and temperature of the cosmic microwave background  $T_{\text{CMB}} = 2.725$  K. The dark matter density is set so that the universe is spatially flat, i.e.,  $\Omega_m = 1 - \Omega_\Lambda$ . Pipelines for the  $N$ -body simulations and ray-tracing are described in [Petri \(2016\)](#), [Zorrilla Matilla et al. \(2016\)](#), and [Liu et al. \(2016\)](#). Specifications of the simulations are also listed on the website of the Columbia Lensing team.

**Neutrino mass simulations (MassiveNuS):** Generated by [Liu et al. \(2018\)](#), this dataset contains convergence maps for several source redshifts created from 101  $\Lambda$ CDM simulations with different  $M_\nu$ ,  $\Omega_m$ , and  $A_s$  (equivalent to  $M_\nu$ ,  $\Omega_m$ , and  $\sigma_8$ ). Other cosmological parameters are fixed:  $\Omega_b = 0.046$ ,  $h = 0.70$ ,  $n_s = 0.97$ ,  $w = -1$ . Each simulation was run in a 512 Mpc/h box with  $1024^3$  particles and used to generate 10,000 convergence maps with  $3.5 \times 3.5$  deg<sup>2</sup> field of view and  $512^2$ -pixel resolution. The fiducial cosmology has parameters  $(M_\nu, \Omega_m, A_s) = (0.1 \text{ eV}, 0.3, 2.1 \times 10^{-9})$ . One cosmology with massless neutrinos  $(M_\nu, \Omega_m, A_s) = (0 \text{ eV}, 0.3, 2.1 \times 10^{-9})$  is used to calculate the covariance matrix of summary statistics. In this study, we will use the convergence maps for 5 source redshifts ( $z = 0.5, 1.0, 1.5, 2.0, \text{ and } 2.5$ ), in 28 cosmologies that are close to the fiducial cosmology, i.e. in the range of  $A_s \in [1.8, 2.7] \times 10^{-9}$ ,  $M_\nu \in [0.06, 0.60] \text{ eV}$ ,  $\Omega_m \in [0.28, 0.32]$ . This range of parameters is enough for estimating the scattering coefficients' constraining power for cosmological parameters in a Rubin-observatory-like survey.

In real lensing surveys, the galaxy shape noise will dilute cosmological information on small scales, acting as a scale cut. It can be approximated by Gaussian white noise on convergence maps ([van Waerbeke 2000](#)),  $\sigma_{\text{noise}}^2 = \langle \sigma_\epsilon^2 \rangle / n_{\text{gal}} A_{\text{pix}}$ , where  $A_{\text{pix}}$  is the pixel area. We adopt an averaged ellipticity squared  $\langle \sigma_\epsilon^2 \rangle = 0.3^2$  and a number density of background galaxies  $n_{\text{gal}}$  of 44 per arcmin<sup>2</sup> to simulate the weak lensing survey of the Rubin Observatory ([LSST Science Collaboration et al. 2009](#)). The multiple source redshifts of the MassiveNuS convergence maps also allow us to explore the information gain from redshift tomography. We consider two situations: (1) only the convergence maps for source redshift  $z = 1$  are used, with  $n_{\text{gal}} = 44$  per arcmin<sup>2</sup>; (2) convergence maps for five source redshifts are used, with  $n_{\text{gal}} = 8.83, 13.25, 11.15, 7.36, \text{ and } 4.26$  per arcmin<sup>2</sup>, respectively, to be consistent with the Rubin Observatory survey ([LSST Science Collaboration et al. 2009](#)). For noisy maps, we also carry out a smoothing with Gaussian kernel  $\sigma = 1$  arcmin.

### 3.2 Summary statistics

We calculate three sets of summary statistics from the simulated lensing convergence maps:

- the binned power spectrum  $P(l)$  which we sample with 30 linear bins of scale,
- the binned bispectrum  $B(l_1, l_2, l_3)$  which we sample with 10 linear bins for each of  $l_1, l_2$ , and  $l_3$  in the bispectrum monopole  $B(l_1, l_2, l_3)$ , resulting in 125 coefficients, and
- the reduced scattering coefficients  $s_1^j$  and  $s_2^{j_1, j_2}$ .

For the scattering coefficients, we use the same Morlet wavelets as described in [Cheng et al. \(2020\)](#), with 4 azimuthal orientations ( $L = 4$ ) and 8 dyadic scales ( $J = 8$ ). The scales correspond to 8 logarithmic

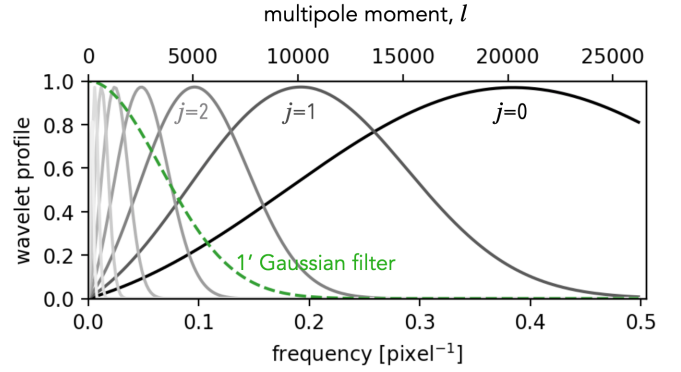


**Figure 3.** Scale coverage of wavelets used by the scattering transform. We also show the profile of a 1 arcmin Gaussian filter in frequency space for comparison.

mic bins from  $l = 100$  to 37,000, as shown in Figure 3. Following Equation 7, we average over the azimuthal orientations and use the 36 reduced scattering coefficients  $s_1$  and  $s_2$ . On noisy maps, the small- $j$  (small scale, high- $l$ ) scattering coefficients are dominated by noise, and we verify that abandoning the small- $j$  coefficients does not change the precision of cosmological inference. As a result, the set of informative scattering coefficients on noisy maps is even more compact than on noiseless maps, which is desirable for inference analysis. As these scattering coefficients are non-negative, we also take the logarithm of them. This step helps to Gaussianize their PDF. We have checked the influence of this step to the cosmological constraints, and found negligible effects.

In summary, for each  $3.5 \times 3.5$  deg<sup>2</sup> lensing map, we calculate 36 scattering coefficients, 30 binned power spectrum coefficients, and 125 binned bispectrum coefficients for the cosmological parameter inference. We have developed a python3 package optimized in speed to calculate the translation-invariant scattering coefficients. The package, together with codes calculating the bispectrum, are available online<sup>4</sup>. We estimated the power spectrum using the `Lenstools` python package ([Petri 2016](#)).

### 3.3 Likelihood and parameter inference

Parameter inference requires a likelihood function. We first assume that the function form of likelihood is Gaussian, i.e., the probability distribution function of the summary statistics is a multivariate Gaussian distribution for a given cosmology. We also assume the cosmological dependence of the mean vector of the Gaussian likelihood can be approximated by a smooth function in the range of interest. For the dark energy dataset, we use a linear dependence, because it has only 7 cosmologies. For the MassiveNuS dataset, we use second-order polynomials. We set the covariance matrix to be independent of cosmology. The latter assumption is conservative but robust when the likelihood is not exactly Gaussian ([Carron 2013](#)). The cosmological dependence of mean vector and the covariance matrix are estimated using the simulated convergence maps.

Given the likelihood, we use the Fisher matrix and Bayesian posterior to quantify the constraining power of lensing scattering coefficients for cosmological parameters. Mathematical formulations of the inference frameworks are given in Appendix C.

<sup>4</sup> [https://github.com/SihaoCheng/scattering\\_transform](https://github.com/SihaoCheng/scattering_transform)

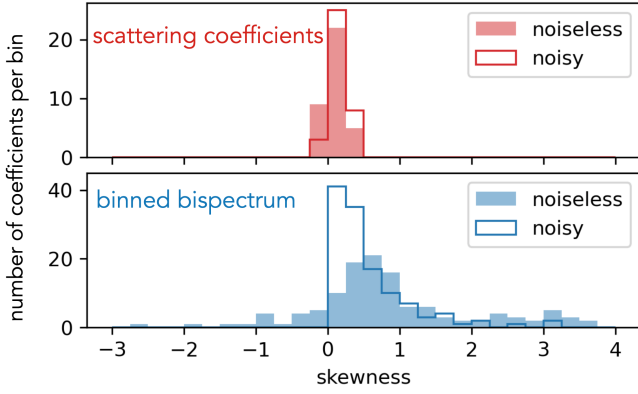


**Figure 4.** Skewness distribution of the scattering and bispectrum coefficients, measured from 10,000 realizations of convergence maps at the fiducial cosmology of MassiveNuS simulation set. If the PDF of these statistical coefficients are Gaussian, then the skewness should be zero.

## 4 RESULTS

### 4.1 The PDF of summary statistics

Before exploring the constraining power on cosmological parameters, we first present one key advantage of using the scattering coefficients, namely their probability density distribution is well Gaussianized.

In the inference framework of many cosmological studies including ours, a Gaussian PDF of statistical estimators is often assumed (also called a Gaussian likelihood assumption). This assumption comes from the central limit theorem when the field of view tends to infinity. However, with a finite field of view, there is no guarantee for a Gaussian likelihood (e.g., Diaz Rivero & Dvorkin 2020; Jeffrey et al. 2021), and approximating a non-Gaussian likelihood with a Gaussian one may introduce bias and/or underestimation of uncertainty to parameter inference (see, e.g., Hahn et al. 2019). Therefore, summary statistics that Gaussianize quickly are favoured.

In Figure 4 we show the skewness distribution of the reduced scattering and binned bispectrum coefficients, calculated on noiseless and noisy maps in the fiducial cosmology of MassiveNuS simulation with source redshift  $z = 1$ . Skewness measures the asymmetry of a PDF, which is one possible deviation from Gaussian distribution. The scattering coefficients<sup>5</sup> have much lower skewness than bispectrum coefficients. We did a similar test for the 95-percentile to measure the heaviness of PDF tails (another possible deviation from Gaussian distribution), which also suggests that the PDFs of scattering coefficients are well Gaussianize, while the bispectrum coefficients are not.

Moreover, we checked the Kullback–Leibler (K–L) divergence (Kullback & Leibler 1951, also see Appendix B) of the scattering and bispectrum coefficients from the corresponding multi-variate Gaussian distribution to be used in the likelihood. The K–L divergence can measure the similarity of a multi-variate data sample to a theoretical distribution. The K–L divergence has a lower bound of zero. Lower K–L divergence means better consistency, though in practice one can never get a zero because of the finite sample size. The scattering coefficients have K–L divergence of 5.83 (noiseless) or 5.68 (noisy). For reference, a numerical experiment using Gaussian

<sup>5</sup> Precisely speaking, we used the logarithm of scattering coefficients, which is allowed because they are positive definite. But, even without taking logarithm, the skewness of scattering coefficients are still small (within [0, 1]).

random variables with the same sample size and dimension yields  $5.46 \pm 0.11$ , just slightly lower than the scattering coefficients. In contrast, the binned bispectrum coefficients have K–L divergence of 38.7 (noiseless) or 30.5 (noisy), much higher than its Gaussian reference ( $17.0 \pm 1.4$ ), meaning that the PDF of these binned bispectrum coefficients deviates significantly from a Gaussian distribution.

In summary, we find that the scattering coefficients Gaussianize particularly well, which is desirable and necessary for accurate cosmological inference.

### 4.2 Constraining cosmological parameters

Having checked the Gaussian likelihood assumption for the scattering coefficients, now we compare the cosmological constraints obtained by different summary statistics. These constraints were obtained based on simulated convergence maps with varied cosmological parameters, and 1,000 (for the dark energy simulation set) or 10,000 (for the neutrino mass simulation set MassiveNuS) realizations for each cosmology.

Because the convergence maps have a long-tailed PDF (approximately log-normal), we do expect the scattering coefficients to extract more information than the bispectrum. Indeed, we find a significantly tighter constraint using the scattering coefficients on noiseless maps (when all high- $l$  modes are included). In Figure 5 we show the Fisher forecast of cosmological parameters using noiseless convergence maps, which corresponds to  $l$  from 100 to roughly 30,000. For simplicity, we only show a plane of two parameters for each dataset. In both panels of Figure 5, the marginalized ellipses are the projection of the three-parameter Fisher ellipsoids onto the plane, while the conditioned ellipses are their cross-sections.

For dark energy parameters (left panel), the power spectrum constrains  $w_0$  well when  $w_a$  is known (conditioned), but constrains poorly if  $w_a$  is also to be constrained (marginalized), meaning a strong degeneracy between  $w_0$  and  $w_a$ . Compared to the bispectrum, which is known to partly break this degeneracy (Takada & Jain 2003), the scattering coefficients almost eliminate it in the noiseless case. In weak lensing cosmology, there is another well-known degeneracy between  $\Omega_m$  and  $\sigma_8$ , which the scattering coefficients can also break (Cheng et al. 2020). However, the dark energy dataset used in this study has a fixed  $\sigma_8$  value. So, it remains to be investigated whether or not the scattering coefficients can break both degeneracies at the same time.

On the noiseless maps, scattering coefficients also provide much tighter constraint on the neutrino mass sum  $M_\nu$  than the power spectrum and bispectrum (see the right panel of Figure 5). In the parameter space spanned by  $\Omega_m$ ,  $\sigma_8$ ,  $M_\nu$ , the power spectrum’s constraining power comes mainly from its overall amplitude, which results in a disc-like Fisher ellipsoid. Adding the bispectrum reduces the disc’s area by partly breaking the  $\Omega_m$ – $\sigma_8$  degeneracy, whereas adding the scattering coefficients almost eliminate it, reducing it to a one-dimension instead of two-dimension degeneracy. This is consistent with the finding presented in the figure 5 of Cheng et al. (2020). The ratio between the volumes of the three-parameter Fisher ellipsoids (i.e., the square root of determinant of the covariance matrix) shown in the right panel of Figure 5 is roughly 20:4:1.

When the galaxy shape noise is taken into account, the constraining power of all summary statistics weakens due to the loss of small scale (high- $l$ ) information. In Figure 6 we show the forecast of neutrino mass sum ( $M_\nu$ ) for a Rubin-observatory-like survey, using the Bayesian posterior with fiducial cosmology at  $(M_\nu, \Omega_m, A_s) = (0.1 \text{ eV}, 0.3, 2.1 \times 10^{-9})$ . In spite of noises, there are still substantial non-Gaussian structures in the lensing convergence maps, thus the scatter-

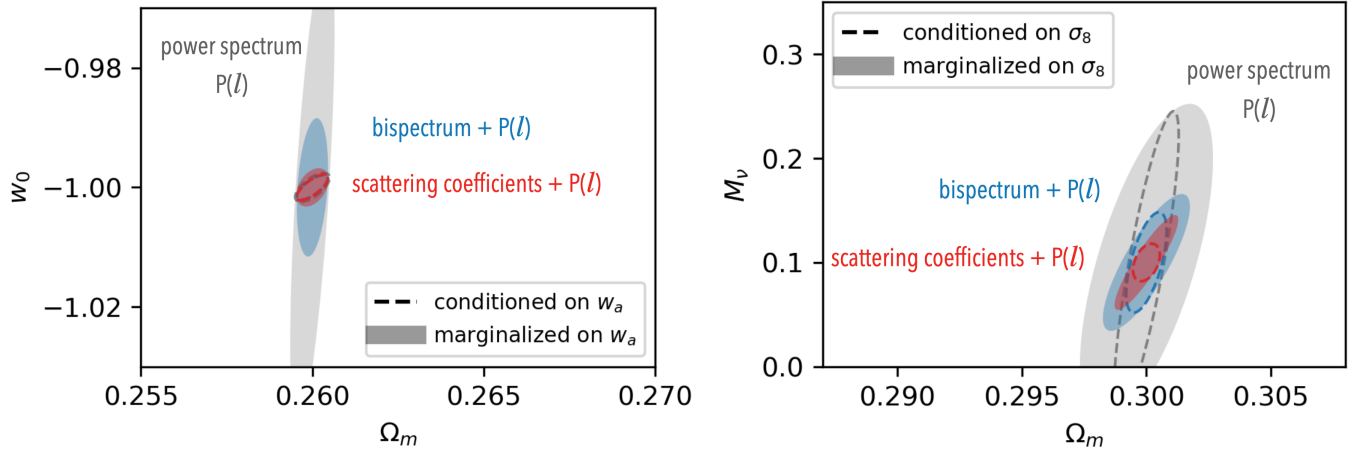


**Figure 5.** Fisher forecast with noiseless  $\kappa$  maps (95% confidence ellipses). The scattering coefficients have remarkably high constraining power for cosmological parameters. *Left:* Forecast for dark energy equation of state index  $w(a) = w_0 + (1 - a)w_a$ , from 20,000  $\text{deg}^2$  noiseless map with  $l$  nominally up to roughly 30,000 and source redshift  $z = 2$ . *Right:* Forecast for neutrino mass  $M_\nu$ , from 20,000  $\text{deg}^2$  noiseless map with source redshift  $z = 1$ .

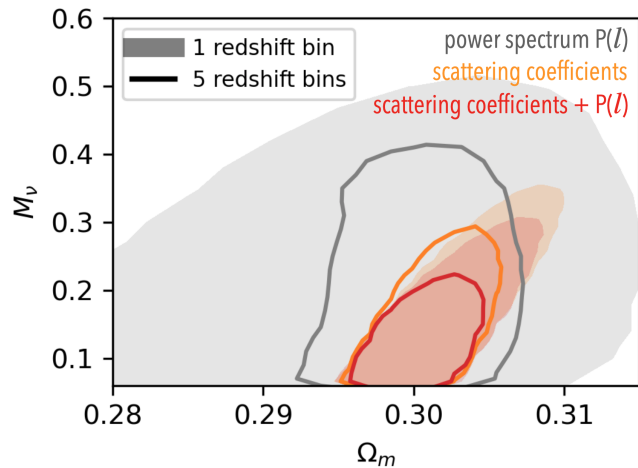


**Figure 6.** Forecast of cosmological parameters (95% confidence contours) for a Rubin-observatory-like survey with 20,000  $\text{deg}^2$  field of view, with  $M_\nu$ ,  $\Omega_m$ , and  $A_s$  (or  $\sigma_8$ ) to be constrained. Colours represent results of different sets of summary statistics of lensing convergence ( $\kappa$ ). Improvement from adding redshift tomography is also shown.

ing coefficients still set much tighter cosmological constraints (more than two times in  $M_\nu$ ) than using the power spectrum alone. In this noisy case, the combination of bispectrum and power spectrum sets a similar constraint to the combination of scattering coefficients and the power spectrum (though not shown in the figure). Figure 6 also show the effect of redshift tomography. A five-bin redshift tomography improves the scattering coefficients' constraint for  $M_\nu$  by about 40%.

With the same dataset (MassiveNuS), similar explorations were performed for other non-Gaussian statistics, including the PDF (Liu & Madhavacheril 2019), bispectrum (Coulton et al. 2019), peak count (Li et al. 2019), starlet peak count (Ajani et al. 2020), minima count (Coulton et al. 2020), Minkowski functionals (Marques et al. 2019), and starlet  $l_1$ -norm (Ajani et al. 2021). They all found similar improvement from redshift tomography for their respective summary statistics.

## 5 CONCLUSIONS

In cosmology, substantial information is stored in non-Gaussian structures on small scales, which requires statistics beyond the power spectrum to extract. Motivated by ongoing and upcoming deep surveys, we explore the weak lensing application of a novel and powerful non-Gaussian statistics, called the scattering transform. We extend the constraining forecast of  $\Omega_m$  and  $\sigma_8$  in Cheng et al. (2020) to more cosmological parameters including the dark energy parameters  $w_0$ ,  $w_a$  and neutrino mass  $M_\nu$ . To do so, we use mock convergence maps from two publicly available simulation suites (the dark energy and MassiveNuS sets) made by the Columbia Lensing team.

We first show that using the scattering coefficients, one can generate random images with textures very close to a simulated lensing map, which cannot be achieved by using the power spectrum and bispectrum coefficients. Then, we show that the scattering coefficients provide significantly better constraint for dark energy parameters  $w_0$ ,  $w_a$  and neutrino mass  $M_\nu$  than using power spectrum alone.

For noiseless maps (when high- $l$  modes are accessible), the scattering transform also outperforms the bispectrum and power spectrum. This result can be explained by the ‘first-order’ nature of scattering coefficients which stay proportional to the field intensity, in contrast to higher-order statistics which amplify fluctuations. This *lower-order* nature together with the wavelet weighting strategy makes the scattering transform an efficient tool for extracting cosmological information. Moreover, the *lower-order* nature makes the distribution of scattering coefficients much more Gaussian than higher-order statistics, as shown in figure 4, which is essential for accurate parameter inference.

We also provide a forecast of  $M_\nu$  with a noise level of the Rubin observatory survey, where the scattering coefficients set a 2 times tighter constraint than using the power spectrum alone, and redshift tomography improves the constraint by an additional 40%. Similar forecast for the dark energy parameters is left for future study, due to the redshift limitation of the mock convergence maps. For noisy maps, although the constraining power of the scattering coefficients is not significantly better than the combination of bispectrum and power spectrum, we argue that the scattering coefficients are still preferred, because the likelihood of scattering coefficients is much more Gaussian than bispectrum coefficients.

The scattering transform yields a compact set of *lower-order* sum-

mary statistics that are stable, powerful, and efficient for characterizing non-Gaussian structures. Together with Cheng et al. (2020), we have shown that the scattering transform has great potential to serve as the non-Gaussian summary statistics in observational cosmology.

## ACKNOWLEDGEMENTS

We thank the Columbia Lensing group (<http://columbialensing.org>) for making their suite of mock lensing maps publicly available and NSF for supporting the creation of those maps through grant AST-1210877 and XSEDE allocation AST-140041. We thank Yuan-Sen Ting for his help on image synthesis. S. C. thanks Siyu Yao for her constant inspiration and encouragement.

## DATA AVAILABILITY

The data underlying this article were accessed from the Columbia Lensing group (<http://columbialensing.org>). The derived data generated in this research will be shared on reasonable request to the corresponding author.

## REFERENCES

- Aihara H., et al., 2018a, *PASJ*, 70, S4  
 Aihara H., et al., 2018b, *PASJ*, 70, S8  
 Ajani V., Peel A., Pettorino V., Starck J.-L., Li Z., Liu J., 2020, *Phys. Rev. D*, 102, 103531  
 Ajani V., Starck J.-L., Pettorino V., 2021, *A&A*, 645, L11  
 Allys E., Levrier F., Zhang S., Colling C., Regaldo-Saint Blancard B., Boulanger F., Hennebelle P., Mallat S., 2019, *A&A*, 629, A115  
 Allys E., Marchand T., Cardoso J. F., Villaescusa-Navarro F., Ho S., Mallat S., 2020, *Phys. Rev. D*, 102, 103506  
 Andén J., Mallat S., 2014, *IEEE Transactions on Signal Processing*, 62, 4114  
 Bartelmann M., Schneider P., 2001, *Phys. Rep.*, 340, 291  
 Bruna J., Mallat S., 2013, *IEEE Transactions on Pattern Analysis and Machine Intelligence*, 35, 1872  
 Bruna J., Mallat S., 2019, *Mathematical Statistics and Learning*, 1, 257  
 Bruna J., Mallat S., Bacry E., J.-F. M., 2015, *The Annals of Statistics*, 43, 323  
 Carron J., 2011, *ApJ*, 738, 86  
 Carron J., 2012, *Phys. Rev. Lett.*, 108, 071301  
 Carron J., 2013, *A&A*, 551, A88  
 Carron J., Neyrinck M. C., 2012, *ApJ*, 750, 28  
 Cheng S., Ting Y.-S., Ménard B., Bruna J., 2020, *MNRAS*, 499, 5902  
 Chevallier M., Polarski D., 2001, *International Journal of Modern Physics D*, 10, 213  
 Coulton W. R., Liu J., Madhavacheril M. S., Böhm V., Spergel D. N., 2019, *J. Cosmology Astropart. Phys.*, 2019, 043  
 Coulton W. R., Liu J., McCarthy I. G., Osato K., 2020, *MNRAS*, 495, 2531  
 Diaz Rivero A., Dvorkin C., 2020, *Phys. Rev. D*, 102, 103507  
 Fisher R. A., 1935, *Journal of the Royal Statistical Society*, 98, 39  
 Foreman-Mackey D., Hogg D. W., Lang D., Goodman J., 2013, *PASP*, 125, 306  
 Fu L., et al., 2014, *MNRAS*, 441, 2725  
 Hahn C., Beutler F., Sinha M., Berlind A., Ho S., Hogg D. W., 2019, *MNRAS*, 485, 2956  
 Hartlap J., Simon P., Schneider P., 2007, *A&A*, 464, 399  
 Jeffrey N., Alsing J., Lanusse F., 2021, *MNRAS*, 501, 954  
 Kacprzak T., et al., 2016, *MNRAS*, 463, 3653  
 Kilbinger M., 2015, *Reports on Progress in Physics*, 78, 086901  
 Kullback S., Leibler R. A., 1951, *Ann. Math. Statist.*, 22, 79  
 LSST Science Collaboration et al., 2009, arXiv e-prints, p. [arXiv:0912.0201](https://arxiv.org/abs/0912.0201)

- Laureijs R., et al., 2011, arXiv e-prints, p. [arXiv:1110.3193](https://arxiv.org/abs/1110.3193)  
 Li Z., Liu J., Matilla J. M. Z., Coulton W. R., 2019, *Phys. Rev. D*, 99, 063527  
 Liu J., Madhavacheril M. S., 2019, *Phys. Rev. D*, 99, 083508  
 Liu J., Petri A., Haiman Z., Hui L., Kratochvil J. M., May M., 2015a, *Phys. Rev. D*, 91, 063507  
 Liu X., et al., 2015b, *MNRAS*, 450, 2888  
 Liu J., Hill J. C., Sherwin B. D., Petri A., Böhm V., Haiman Z., 2016, *Phys. Rev. D*, 94, 103501  
 Liu J., Bird S., Zorrilla Matilla J. M., Hill J. C., Haiman Z., Madhavacheril M. S., Petri A., Spergel D. N., 2018, *J. Cosmology Astropart. Phys.*, 2018, 049  
 Mallat S., 2012, *Communications on Pure and Applied Mathematics*, 65, 1331  
 Marques G. A., Liu J., Zorrilla Matilla J. M., Haiman Z., Bernui A., Novaes C. P., 2019, *J. Cosmology Astropart. Phys.*, 2019, 019  
 Martinet N., et al., 2018, *MNRAS*, 474, 712  
 Martinet N., Harnois-Déraps J., Jullo E., Schneider P., 2021, *A&A*, 646, A62  
 Neyrinck M. C., Szapudi I., 2007, *MNRAS*, 375, L51  
 Neyrinck M. C., Szapudi I., Rimes C. D., 2006, *MNRAS*, 370, L66  
 Petri A., 2016, *Astronomy and Computing*, 17, 73  
 Petri A., Liu J., Haiman Z., May M., Hui L., Kratochvil J. M., 2015, *Phys. Rev. D*, 91, 103511  
 Rimes C. D., Hamilton A. J. S., 2005, *MNRAS*, 360, L82  
 Rimes C. D., Hamilton A. J. S., 2006, *MNRAS*, 371, 1205  
 Saydjari A. K., Portillo S. K. N., Slepian Z., Kahraman S., Burkhart B., Finkbeiner D. P., 2020, arXiv e-prints, p. [arXiv:2010.11963](https://arxiv.org/abs/2010.11963)  
 Shan H., et al., 2018, *MNRAS*, 474, 1116  
 Sifre L., Mallat S., 2013, the IEEE Conference on Computer Vision and Pattern Recognition (CVPR), pp 1233–1240  
 Spergel D., et al., 2015, arXiv e-prints, p. [arXiv:1503.03757](https://arxiv.org/abs/1503.03757)  
 Takada M., Jain B., 2003, *ApJ*, 583, L49  
 Tegmark M., Taylor A. N., Heavens A. F., 1997, *ApJ*, 480, 22  
 Vogeley M. S., Szalay A. S., 1996, *ApJ*, 465, 34  
 Zorrilla Matilla J. M., Haiman Z., Hsu D., Gupta A., Petri A., 2016, *Phys. Rev. D*, 94, 083506  
 van Waerbeke L., 2000, *MNRAS*, 313, 524

## APPENDIX A: BINNED BISPECTRUM

Here we describe the formulation of the binned bispectrum. The bispectrum is the products of three Fourier coefficients,

$$B(\mathbf{k}_1, \mathbf{k}_2, \mathbf{k}_3) \equiv \langle \tilde{I}(\mathbf{k}_1) \tilde{I}(\mathbf{k}_2) \tilde{I}(\mathbf{k}_3) \rangle \quad (\text{A1})$$

Because of symmetry, it is enough to consider only cases with  $k_1 < k_2 < k_3$ . Under statistical homogeneity, the coefficients vanish unless  $\mathbf{k}_1 + \mathbf{k}_2 + \mathbf{k}_3 = 0$ . To reduce the number of coefficients, one can use the binned bispectrum mono-pole, which averages the bispectrum according to the magnitude of  $k_1$ ,  $k_2$ , and  $k_3$

$$B_{i,j,k} = \int_{k_i}^{k_{i+1}} d\mathbf{k}_1 \int_{k_j}^{k_{j+1}} d\mathbf{k}_2 \int_{k_k}^{k_{k+1}} d\mathbf{k}_3 \\ (2\pi)^2 \delta^{(2)}(\mathbf{k}_1 + \mathbf{k}_2 + \mathbf{k}_3) \cdot \tilde{I}(\mathbf{k}_1) \tilde{I}(\mathbf{k}_2) \tilde{I}(\mathbf{k}_3) \quad (\text{A2})$$

It is not convenient to select  $\delta(\mathbf{k}_1 + \mathbf{k}_2 + \mathbf{k}_3)$  triplets within each bin. Fortunately, expanding the right-hand side of Eq. A2 in real space will simplify the integrant,

$$B_{i,j,k} = \langle (I \star f_i)(I \star f_j)(I \star f_k) \rangle, \quad (\text{A3})$$

where  $f_i(\mathbf{x}) = \int_{k_i}^{k_{i+1}} e^{i\mathbf{k} \cdot \mathbf{x}} d\mathbf{k}$  is the inverse Fourier transform of the binning, an annulus in Fourier space and a wavelet-like profile in real space. This form of expression, similar to the scattering coefficients, means that the bispectrum (and other  $N$ -point functions) can also be expressed as the spatial mean of some non-linear transformation of the input field, though it has different properties from the scattering one.

**APPENDIX B: KULLBACK–LEIBLER DIVERGENCE**

The K–L divergence can measure the similarity of a data sample to a target distribution. For a discrete situation,

$$D_{\text{KL}}(P||Q) = \sum_i P(x_i) \log \frac{P(x_i)}{Q(x_i)}, \quad (\text{B1})$$

where  $P$  and  $Q$  are the observed and theoretical distribution, respectively. In our case we set  $P$  as  $\frac{1}{N}$ , where  $N$  is the number of sample points, and  $Q$  as the PDF value of Gaussian distribution at the sample points  $x_i$ , normalized over all sample points. A zero K–L divergence means perfect consistency, while a large value means that the data is an unexpected sample of the target distribution, or the data do not likely follow the target distribution. In practice one can never get a zero because of the finite sample size.

**APPENDIX C: COSMOLOGICAL INFERENCE FRAMEWORK**

For a statistical model of observable  $\mathbf{x}$ , the Cramér–Rao inequality sets the lower limit of any unbiased estimators of model parameters obtained from the observable, therefore it can be used to quantify the uncertainty of parameter inference.

$$\text{cov}(\hat{\theta}) \geq \mathbf{I}(\theta)^{-1}, \quad (\text{C1})$$

where  $\mathbf{I}(\theta)$  is the Fisher information matrix, whose elements are defined as

$$I_{m,n}(\theta) \equiv - \left\langle \frac{\partial \ln p(\mathbf{x}|\theta)}{\partial \theta_m} \frac{\partial \ln p(\mathbf{x}|\theta)}{\partial \theta_n} \right\rangle. \quad (\text{C2})$$

In our case,  $\theta$  is the cosmological parameters, and  $\mathbf{x}$  is the vector of summary statistics such as the scattering coefficients. The likelihood is assumed to be Gaussian,

$$p(\mathbf{x}|\theta) \propto \frac{1}{\sqrt{|\mathbf{C}|}} \exp\left[-\frac{1}{2}(\mathbf{x} - \boldsymbol{\mu})^T \mathbf{C}^{-1}(\mathbf{x} - \boldsymbol{\mu})\right], \quad (\text{C3})$$

where  $\mathbf{C}(\theta)$  is the covariance matrix of summary statistics. We further assume  $\mathbf{C}(\theta)$  is cosmology independent. Thus, the Fisher matrix becomes

$$I_{m,n} = \frac{\partial \boldsymbol{\mu}^T}{\partial \theta_m} \mathbf{C}^{-1} \frac{\partial \boldsymbol{\mu}}{\partial \theta_n}. \quad (\text{C4})$$

We use linear or second-order polynomials to fit the cosmological dependence of the mean vector  $\boldsymbol{\mu}(\theta)$ , and use the sample covariance matrix  $\hat{\mathbf{C}}$  estimated from simulations at fiducial cosmologies ( $\Omega_m = 0.26$ ,  $w_0 = -1$ ,  $w_a = 0$  for the dark energy dataset and  $\Omega_m = 0.3$ ,  $M_V = 0$ ,  $A_s = 2.1 \times 10^{-9}$  for the MassiveNuS dataset) to estimate the inverse of covariance matrix (Hartlap et al. 2007):

$$\widehat{\mathbf{C}}^{-1} = \frac{N - D - 2}{N - 1} \hat{\mathbf{C}}^{-1}, \quad (\text{C5})$$

where  $\widehat{\mathbf{C}}^{-1}$  is an unbiased estimator,  $N$  is the number of independent sample used for the estimation (1,000 for the dark energy dataset and 10,000 for the MassiveNuS dataset),  $D$  is the number of summary statistics used, which is 36, 30, and 125 per redshift bin, for scattering coefficients, binned power spectrum, and binned bispectrum, respectively.

The Bayesian posterior is another way to quantify the uncertainty of model parameter inference. Given the likelihood  $p(\mathbf{x}|\theta)$ , the posterior probability distribution of model parameter is

$$p(\theta|\mathbf{x}) \propto p(\mathbf{x}|\theta)p(\theta), \quad (\text{C6})$$

where  $p(\theta)$  is the prior distribution of  $\theta$ . For the noisy cases with MassiveNuS, we use a flat prior in  $\Omega_m \in [0.28, 0.32]$ ,  $M_V \in [0.06, 0.6]$  eV, and  $A_s \in [1.8, 2.7] \times 10^{-9}$  to avoid extrapolation. The posterior is then sampled using emcee (Foreman-Mackey et al. 2013), a Markov Chain Monte Carlo (MCMC) sampler. We used 32 walkers, ran 1,000 steps to burn-in and then 10,000 steps to sample the posterior. Sampling convergence was checked within and among chains.

This paper has been typeset from a  $\text{\TeX}/\text{\LaTeX}$  file prepared by the author.